4

LINEAR STABILITY ANALYSIS OF A COMPRESSIBLE BOUNDARY LAYER COMPUTED BY NAVIER-STOKES CODE

Toshiyuki NOMURA
Aircraft Aerodynamics Division
National Aerospace Laboratory
Tokyo, Japan

1. Introduction

Development of high-accuracy schemes and improvement of computers in the aspects of both operational speed and memory have enabled Navier-Stokes code to compute boundary layers for stability analysis instead of a boundary-layer code. It is therefore important to verify how accurate the boundary layers computed by Navier-Stokes code are.

For numerical simulation of the supersonic flow around an infinite swept cylinder, the number of cells needed in order to eliminate the dependence of the boundary-layer flow on the computational grid is investigated. In comparison between the boundary-layer flow converged by the diagonalized ADI scheme and that converged by the LU-SGS scheme, the way the two kinds of time-marching methods affect the flow is also investigated. And furthermore, the linear stability analysis of the boundary layer at the attachment line is performed.

2. Navier-Stokes Code

The governing equations are the conservation form of the thin-layer Navier-Stokes equations, which are numerically solved by the finite-volume scheme.

$$\frac{\partial \hat{Q}}{\partial t}+\frac{\partial \hat{E}}{\partial \xi}+\frac{\partial \hat{F}}{\partial \eta}+\frac{\partial \hat{G}}{\partial \zeta}=\frac{1}{Re}\frac{\partial \hat{F}_v}{\partial \eta}$$

2.1 Numerical Fluxes

The inviscid fluxes $\hat{E}$, $\hat{F}$ and $\hat{G}$ are computed by the Chakravarthy-Osher TVD scheme[1]. The first-order accurate flux at the cell interface is given by

$$\hat{E}_{j+1/2}=\frac{1}{2}(\hat{E}_j+\hat{E}_{j+1})-\frac{1}{2}T_{\xi,j+1/2}(\hat{\Lambda}^{+}_{\xi,j+1/2}-\hat{\Lambda}^{-}_{\xi,j+1/2})T^{-1}_{\xi,j+1/2}(Q_{j+1}-Q_j),$$

$$\hat{A}=\frac{\partial \hat{E}}{\partial Q}=T_\xi \hat{\Lambda}_\xi T_\xi^{-1},\ \lambda^{\pm}_\xi=\frac{1}{2}(\lambda_\xi \pm |\lambda_\xi|).$$

$\hat{\Lambda}_\xi$ is the diagonal matrix that consists of the eigenvalues λ_ξ of the Jacobian matrix $\hat{A}$, and T_ξ is the similarity-transformation matrix that consists of the right eigenvectors of $\hat{A}$. $\hat{\Lambda}^{+}_\xi$ is the matrix where λ_ξ in $\hat{\Lambda}_\xi$ are replaced by λ^{+}_ξ, and $\hat{\Lambda}^{-}_\xi$ is the matrix where λ_ξ in $\hat{\Lambda}_\xi$ are replaced by λ^{-}_ξ. Density, velocities and enthalpy at the cell interface are computed using Roe's special averaging procedure. The accuracy of the above flux can be raised to the third order by adding the correction terms with the minmod limiter.

The viscous flux $\hat{F}_v$ is computed on the basis of Gauss's theorem.

2.2 Diagonalized ADI Scheme

The diagonalized ADI scheme by Pulliam and Chaussee[2] can be written as

$$T_\xi(I+\frac{\Delta t}{V}D_\xi\hat{\Lambda}_\xi)T_\xi^{-1}T_\eta(I+\frac{\Delta t}{V}D_\eta\hat{\Lambda}_\eta)T_\eta^{-1}T_\zeta(I+\frac{\Delta t}{V}D_\zeta\hat{\Lambda}_\zeta)T_\zeta^{-1}\Delta Q=-\frac{\Delta t}{V}\hat{R},$$

$$\hat{A}=\frac{\partial \hat{E}}{\partial Q}=T_\xi\hat{\Lambda}_\xi T_\xi^{-1},\ \hat{B}=\frac{\partial \hat{F}}{\partial Q}=T_\eta\hat{\Lambda}_\eta T_\eta^{-1},\ \hat{C}=\frac{\partial \hat{G}}{\partial Q}=T_\zeta\hat{\Lambda}_\zeta T_\zeta^{-1},$$

$$\hat{R}=D_\xi\hat{E}+D_\eta\hat{F}+D_\zeta\hat{G}-\frac{1}{Re}D_\eta\hat{F}_v.$$

D is a difference operator. The left hand of the ADI scheme is a block-tridiagonal system, and meanwhile the left hand of the diagonalized ADI scheme is a scalar-tridiagonal one. That makes the fast inversion of the left hand possible.

2.3 LU-SGS Scheme

The LU-SGS scheme by Yoon and Jameson[3] can be written as

$$L D^{-1} U \Delta Q = -\frac{\Delta t}{V}\hat{R},$$

$$L = I + \frac{\Delta t}{V}(D_\xi^- \hat{A}^+ + D_\eta^- \hat{B}^+ + D_\zeta^- \hat{C}^+ - \hat{A}^- - \hat{B}^- - \hat{C}^-),$$

$$D = I + \frac{\Delta t}{V}(\hat{A}^+ - \hat{A}^- + \hat{B}^+ - \hat{B}^- + \hat{C}^+ - \hat{C}^-),$$

$$U = I + \frac{\Delta t}{V}(D_\xi^+ \hat{A}^- + D_\eta^+ \hat{B}^- + D_\zeta^+ \hat{C}^- + \hat{A}^+ + \hat{B}^+ + \hat{C}^+),$$

$$\hat{A}^\pm = \frac{1}{2}[\hat{A} \pm \rho_\xi I], \hat{B}^\pm = \frac{1}{2}[\hat{B} \pm \rho_\eta I], \hat{C}^\pm = \frac{1}{2}[\hat{C} \pm \rho_\zeta I],$$

$$\rho_\xi = \kappa max[|\lambda_\xi|], \rho_\eta = \kappa max[|\lambda_\eta|], \rho_\zeta = \kappa max[|\lambda_\zeta|].$$

κ is a constant that is greater than or equal to 1. D^- is a backward-difference operator, and D^+ is a forward-difference operator. The approximation of the Jacobian matrices not only improves the stability of the scheme but substantially removes the inversion of the left hand.

2.4 Computational Grid

Three kinds of C-type grids, which differ in density, are generated for the infinite cylinder with a swept angle of 60° shown in Fig. 1. Grid B of medium density is shown in Fig. 2. The grid generator is based on Takanashi's method[4]. The number of grid points, the minimum spacing in the attachment-line boundary layer, the Courant number and the time steps for convergence are tabulated in Table 1 for each grid. The time-marching method used is the diagonalized ADI scheme.

The Mach number of the free stream is 3.5, and the Reynolds number based on the diameter of the cylinder is 1.05×10^6.

3. Linear Stability-Analysis Code

The nonconservation form of the Navier-Stokes equations in Cartesian coordinates is linearized by substituting fluctuation quantities into it, and then the parallel-flow approximation is made. Assuming the fluctuation quantities normal-mode, stability equations are obtained that can be written as

$$[\tilde{u}(y), \tilde{v}(y), \tilde{w}(y), \tilde{p}(y), \tilde{\tau}(y)]\, e^{i(\alpha x + \beta z - \omega t)},$$

$$(AD^2 + BD + C)\vec{\phi} = 0, \vec{\phi} = (\alpha\tilde{u} + \beta\tilde{w}, \tilde{v}, \tilde{p}, \tilde{\tau}, \alpha\tilde{w} - \beta\tilde{u})^T, D \equiv d/dy.$$

τ is temperature. A, B and C are 5×5 matrices computed on the basis of the velocity profiles and temperature one in the boundary layer. Here the temporal stability is dealt with. α and β are the real wavenumbers specified, and ω is the complex frequency unknown. The Malik-Orszag global method[5] is applied to the stability equations, and then ω is obtained.

4. Results

The dependence of the boundary-layer flow on the computational grid is investigated, and the effect of the time-marching method on the flow is also investigated. And furthermore, the linear stability analysis of the boundary layer at the attachment line is performed.

4.1 Dependence of the Boundary-Layer Flow on the Grid

The boundary-layer flows computed with each grid are compared. The time-marching method used is the diagonalized ADI scheme that includes the local time step with the constant Courant number shown in Table 1.

The velocity and temperature profiles at the position of $\theta = 0°$ are shown in Fig. 3. Grid A has 8 cells between the wall and the boundary-layer edge, Grid B 14 cells, and Grid C 28 cells. Though Grid A appears coarse, the physical quantities at the cell centers coincide with those obtained with the other grids except near the wall. There is no

difference between the profiles of Grid B and Grid C.

The velocity and temperature profiles at the position of $\theta = 90°$ are shown in Fig. 4. Grid A has 9 cells between the wall and the boundary-layer edge, Grid B 17 cells, and Grid C 32 cells. The velocity profiles of Grid A slightly deviate from the others. The temperature profile of Grid A is a little higher near the wall than the others. There is no difference between the profiles of Grid B and Grid C.

In consequence, Grid B appears to have enough density to eliminate the dependence of the boundary-layer flow on the grid.

4.2 Effect of the Time-Marching Method on the Boundary-Layer Flow

A comparison is made between the boundary-layer flow converged by the diagonalized ADI scheme and that converged by the LU-SGS scheme. The LU-SGS scheme includes the local time step with the Courant number of 1, and the time is marched by 4000 steps. Grid B is employed in both cases.

The velocity and temperature profiles at the position of $\theta = 0°$ are shown in Fig. 5. There is no difference between the two velocity profiles, and meanwhile the temperature profile converged by the LU-SGS scheme is a little higher near the wall than that converged by the diagonalized ADI scheme.

The velocity and temperature profiles at the position of $\theta = 90°$ are shown in Fig. 6. The two velocity profiles coincide with each other precisely, and the same can be said of the temperature profiles.

In consequence, the usage of the two different time-marching methods yields very little difference between the converged flows.

4.3 Linear Stability Analysis of the Boundary Layer at the Attachment Line

The temporal stability is investigated for the laminar boundary layer at the attachment line. The boundary layer is computed using Grid B and the diagonalized ADI scheme. The wavenumber vector of the disturbances is inclined at 60° from Z coordinate. The obtained ranges, where the disturbances grow, are shown in Fig. 7 with the neutral-stability curves by Malik[6]. Both are in good agreement, which shows that the boundary layer is accurate enough to perform the stability analysis. F, $\bar{R}$ and ζ in Fig. 7 are defined as

$$F = \frac{2\pi\nu_e}{W_e^2} f, \quad \bar{R} = \frac{W_e \zeta}{\nu_e}, \quad \zeta = \left[\frac{\nu_e}{dU_e/dX}\right]_{X=0}^{1/2},$$

where e refers to the conditions at the boundary-layer edge.

5. Conclusions

The compressible boundary-layer flow on an infinite swept cylinder is computed by Navier-Stokes code with the grid density changed or with the time-marching method replaced. The dependence of the boundary-layer flow on the grid appears to be eliminated by employing a grid as dense as Grid B. There is very little difference between the boundary-layer flow converged by the diagonalized ADI scheme and that converged by the LU-SGS scheme. And furthermore, the results of the stability analysis of the boundary layer at the attachment line agree fairly well with those obtained by Malik.

References

[1] Chakravarthy, S. R., "Development of Upwind Schemes for the Euler Equations," NASA CR 4043, 1987.

[2] Pulliam, T. H. and Chaussee, D. S., "A Diagonal Form of an Implicit Approximate-Factorization Algorithm," J. Comp. Phys., Vol. 39, pp. 347-363, 1981.

[3] Yoon, S. and Kwak, D., "An Implicit Three-Dimensional Navier-Stokes Solver for Compressible Flow," AIAA Paper 91-1555-CP, June 1991.

[4] Takanashi, S. and Takemoto, M., "A Method of Generating Structured-Grids for Complex Geometries and Its Application to the Navier-Stokes Simulation," CFD J., Vol. 2, No. 2, pp. 209-218, 1993.

[5] Malik, M. R., " Finite-Difference Solution of the Compressible Stability Eigenvalue Problem," NASA CR 3584, 1982.

[6] Malik, M. R. and Beckwith, I. E., " Stability of a Supersonic Boundary Layer along a Swept Leading Edge," AGARD CP 438, pp. 3-1 to 3-9, 1988.

	Points($\xi \times \eta$)	Min. spacing(y^+)	Courant no.	Time steps
Grid A	112× 46	1.658471	1	4000
Grid B	224× 91	0.4233750	2	4000
Grid C	448×181	0.1064922	8	6000

Table 1: Computational grids

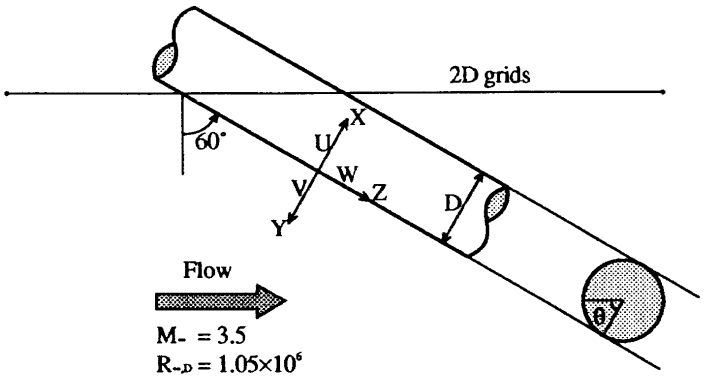

Fig. 1: Infinite swept cylinder

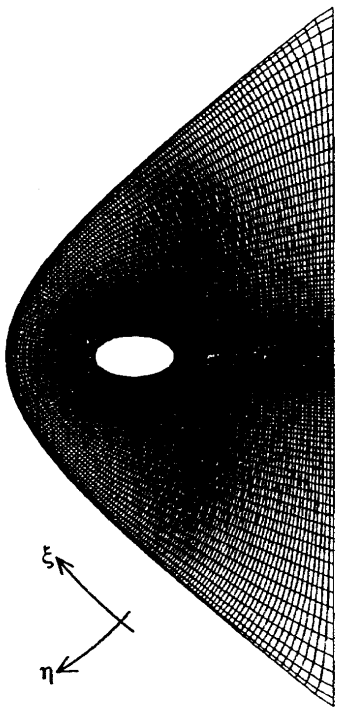

Fig. 2: Grid B (224 × 91)

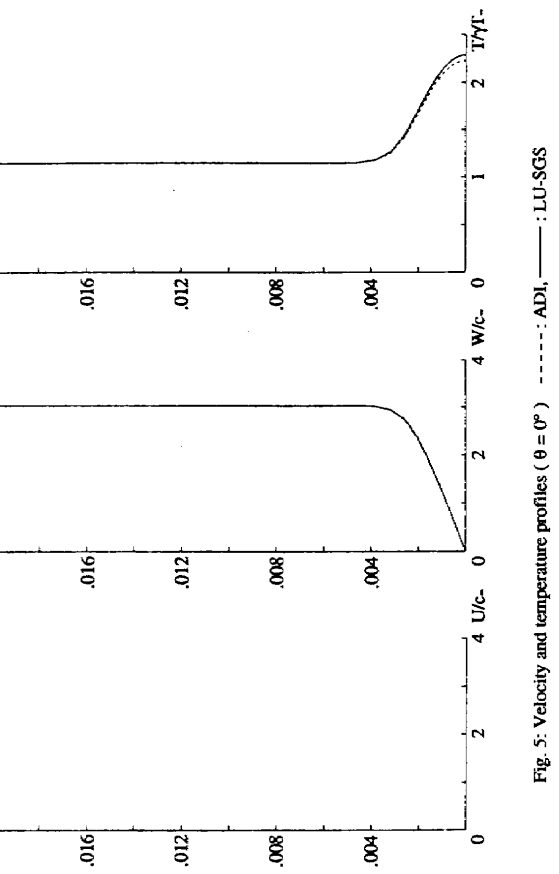

Fig. 3: Velocity and temperature profiles (θ = 0°) -------: Grid A, — - — - : Grid B, ——— : Grid C

Fig. 5: Velocity and temperature profiles (θ = 0°) - - - - - : ADI, ——— : LU-SGS

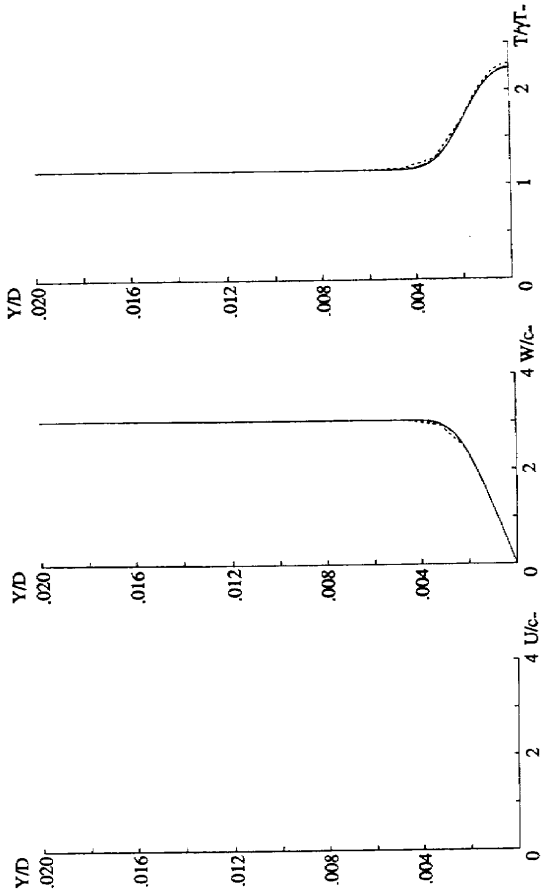

Fig. 4: Velocity and temperature profiles (θ = 90°) -------: Grid A, — - — - : Grid B, ——— : Grid C

Fig. 6: Velocity and temperature profiles (θ = 90°) - - - - - : ADI, ——— : LU-SGS

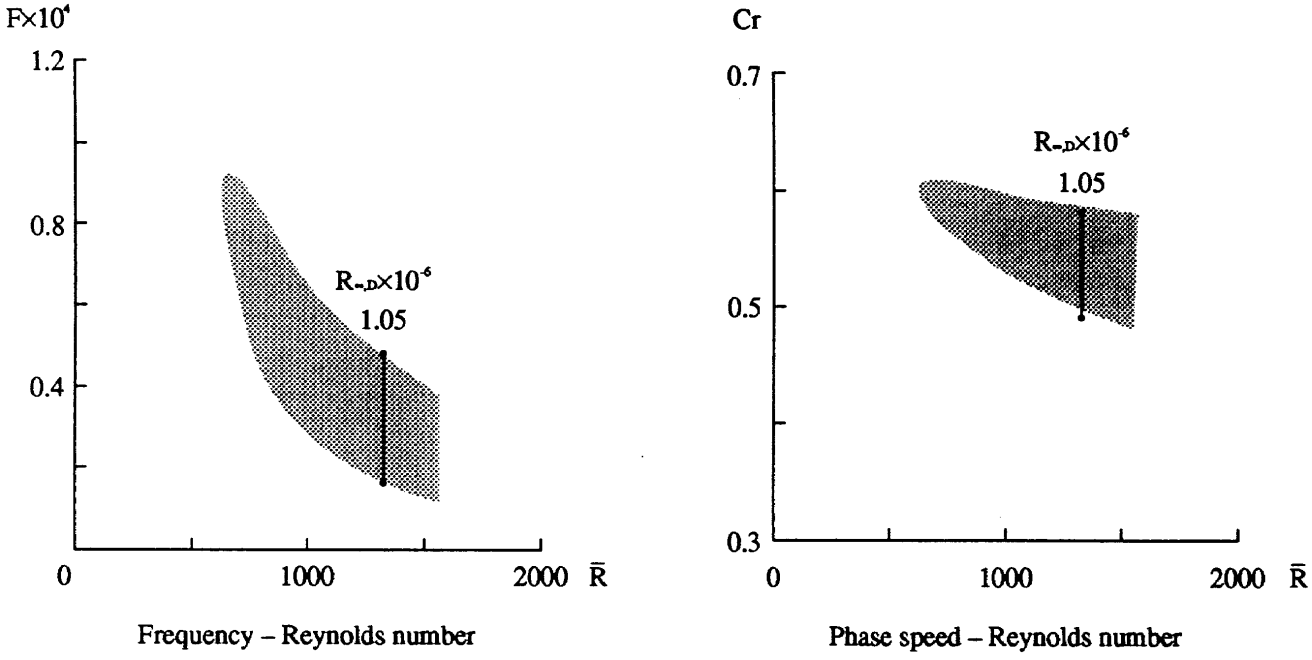

Fig. 7: Unstable ranges